aerospace

MDPI

Article

Research on Micro Gap Flow Field Characteristics of Cylindrical Gas Film Seals Based on Experimental and Numerical Simulation

Zhen Xu [1], Lianjiang Xu [1], Junfeng Sun [2,*], Meihong Liu [2], Taohong Liao [3] and Xiangping Hu [4,*]

[1] Faculty of Mechanical and Electrical Engineering, Yunnan Open University, Kunming 650500, China; 15925163096@139.com (Z.X.); 13888673055@163.com (L.X.)
[2] Faculty of Mechanical and Electrical Engineering, Kunming University of Science and Technology, Kunming 650504, China; 13648861980@163.com
[3] Department of Marine Technology, Norwegian University of Science and Technology, 7491 Trondheim, Norway; liao.taohong@gmail.com
[4] Industrial Ecology Programme, Department of Energy and Process Engineering, Norwegian University of Science and Technology, 7491 Trondheim, Norway
* Correspondence: junfengsun@139.com (J.S.); xiangping.hu@ntnu.no (X.H.)

Abstract: Flexible support cylindrical gas film seals (CGFSs) adapt well to rotor whirling and have a good gas lubrication effect during thermal deformation. However, when a CGFS operates under the "three high" (high interface slip speed, high-pressure differential, and high ambient temperature) operating conditions, the complex deformation of the support structure is a crucial factor affecting the stability of the CGFS. A thorough and systematic analysis of the micro gap flow field characteristics of flexible support CGFSs is a fundamental problem when we study the deformation of the support structure under multiple physical field conditions. This study uses a cylindrical gas film high-speed rotor test rig to study and compare the sealing characteristics of experiments and numerical simulations and then optimizes and verifies the accuracy and effectiveness of the simulation model. A cross-scale gas film grid model is used to analyze the flow field characteristics and seal ability of different groove models and compare the mechanical characteristics and sealing performance. We also analyze the gas film pressure distribution in micro gaps and explore the impact of dynamic pressure groove microstructure on flow field characteristics. Results show that micro gaps are the primary conditions for generating hydrodynamic effects, and high rotational speed, high-pressure differential, and large eccentricity have a significant effect on improving hydrodynamic effects and enhancing gas film stability. However, an increase in these parameters can cause an increase in leakage rate. A single flow channel makes it easier to improve the hydrodynamic effect, gas film load-bearing ability, and gas film stability while reducing leakage rate. The analyses in this study supplement and improve the theory of the flow field characteristics of cylindrical annular micro gaps and provide a theoretical basis for exploring the relation between the support structural parameters of the CGFS and the mechanical characteristics of the micro gap flow field. This study provides important guidance to the establishment of a quantitative design theory of supporting structures.

Keywords: cylindrical gas film seal; gas model structural parameters; operating parameters; aerodynamic characteristics micro gap flow field

Citation: Xu, Z.; Xu, L.; Sun, J.; Liu, M.; Liao, T.; Hu, X. Research on Micro Gap Flow Field Characteristics of Cylindrical Gas Film Seals Based on Experimental and Numerical Simulation. *Aerospace* **2024**, *11*, 40. https://doi.org/10.3390/aerospace11010040

Academic Editor: Pietro Catalano

Received: 1 December 2023
Revised: 25 December 2023
Accepted: 27 December 2023
Published: 29 December 2023

1. Introduction

Improving the efficiency of aviation gas turbines is an effective way to reduce carbon emission and pollutant emissions. However, the layout design of the aero engine gas path system is complete, and it is difficult to reduce engine fuel consumption by improving and optimizing the structure of aviation engines. The adoption of advanced sealing technology has a significant impact on stable operation, efficiency improvement, and consumption reduction in high-speed rotor systems [1–4].

NASA research shows that advanced dry gas sealing technology can enhance engine life under harsh operating conditions and reduce engine fuel consumption [2,5,6]. Flexible support cylindrical gas film seals (CGFSs) can adapt to the high interface slip velocity, high boundary pressure differential, and high ambient temperature conditions of the aircraft engine. At the same time, the flexible support system of the CGFS can effectively overcome the large deformation caused by the thermal deformation of the rotor [7–12]. Zhang et al. analyzed the impact of working condition parameters and groove parameters on the gas pressure and gas velocity of the fluid domain, and they studied the impact of these two parameters on the dynamic sealing performance of a CGFS, the leakage of the cylindrical gas film dynamic pressure sealing device was tested at different rotary speed [13]. In order to form a stable gas film with high gas film stiffness during high-speed rotation, a series of shallow grooves, called dynamic pressure grooves, are generally required to be engraved on the gas film seal runway. Bahukudumbi et al. [14,15] found the sealing performance of grooved structures is better than that of non-grooved structures. Therefore, the grooves on the sealing components have great research value [16]. Currently, common groove structures include T-grooves, straight grooves, spiral grooves, etc. [17]. Ding et al. studied the sealing performance of a micro gap floating ring using the CFD analysis method. At the same time, a comparative analysis was conducted on the internal flow field of the two types of gas film seals, the no-groove floating ring and the spiral groove floating ring [18,19]. In 2021, Zhao et al. carried out fluid–structure interaction analysis on the gas film flow field and flexible support system of T-groove CGFSs using the FEM method, and they found that bubbling type support components can improve the system stability of a CGFS [20]. Sun et al. proposed a new CGFS form with a flexible support structure based on the characteristics of fluid dynamic sealing conditions and established a cylindrical gas film analysis model with a flexible wave foil. They also used CFD to analyze the 3D flow field gas film model and studied the impact of sealing operating parameters and gas model structural parameters of the gas film on the sealing steady-state characteristics [21,22]. Hou et al. analyzed the impact of rotor eccentricity and centrifugal expansion effect on the performance of a compliant cylindrical intershaft gas film seal and proposed an analysis method for gas film pressure. However, in the study of operating parameters, the impact of eccentricity and rotational speed on sealing performance was mainly considered [23,24]. Wang et al. designed a groove bottom diversion texture and studied the influence of diversion texture on the sealing performance of cylindrical gas film seals under different working conditions. The research results showed that diversion texture is beneficial for improving the effectiveness and stability of cylindrical gas film seals. However, the calculation model used in this study has some errors under large eccentricity. At the same time, the research conclusions lack validation [25].

When numerical analysis methods are applied to study cylindrical gas film, cross-scale characteristics, mesh generation, and mathematical model selection are the crucial factors affecting the accuracy of the results. However, most researchers have mainly made macro analyses on the gas pressure and gas leakage in the micro gap. There are few microscopic descriptions and research studies on the distribution law of gas pressure in the dynamic pressure grooves. In addition, there is a lack of experimental verification in some research studies on CGFSs, which may lead to biased results. Therefore, this study evaluates the inherent laws of the microstructure of the dynamic pressure groove and pressure distribution and the mechanical characteristics of the micro gap flow field. This study considers the operating conditions of CGFSs and uses a compressible ideal gas model for analysis and calculation, fully considering the impact of large pressure differential and temperature on gas density and accurately analyzing the impact of operating parameters on sealing performance. The research conducted in this study is of great significance for the design and optimization of dynamic pressure grooves, as well as for improving the performance of CGFSs.

2. Sealing Structure and Parameter Setting

2.1. Design of CGFS

Figure 1 is the structural schematic diagram of the flexible support CGFS designed in this article. The CGFS shown in Figure 1 mainly includes a floating ring, a moving ring, a flexible support, a static ring, a shaft sleeve, a spring, and a stator. The outer cylindrical surface of the moving ring is machined with dynamic pressure grooves. When the shaft rotates, a very small gap is formed between the stationary floating ring and the rotating ring. The gas at the sealing inlet will be pumped into the gap, and the gas will be continuously compressed to form a hydrodynamic effect. This forms a gas film with extremely thin thickness and very high gas film stiffness, to achieve the sealing of the leakage channel. Due to the eccentricity, a convergent wedge-shaped gap with varying thickness is formed and it will further enhance the hydrodynamic effect and greatly improve the bearing capacity of the gas film.

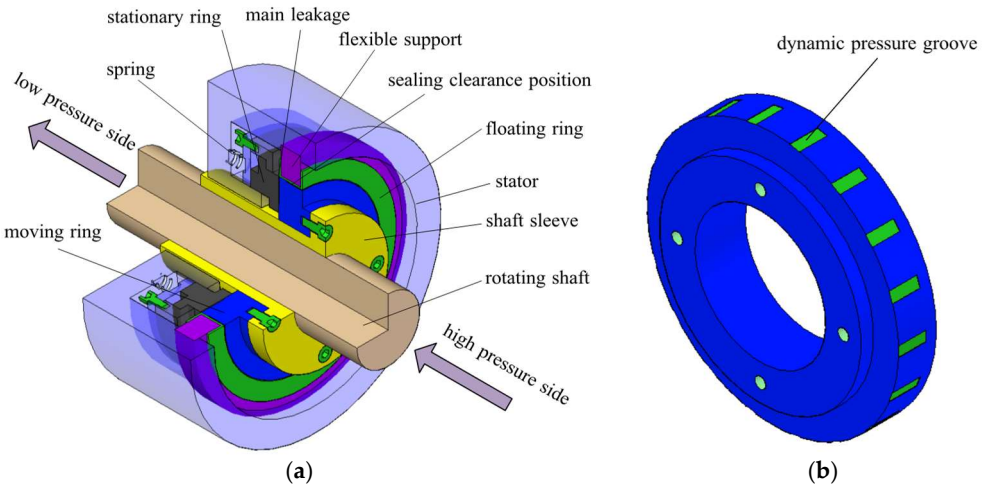

Figure 1. Schematic diagram of flexible support CGFS. (**a**) Schematic diagram of sealing assembly; (**b**) schematic diagram of moving ring.

2.2. Theoretical Equation

Figure 2 shows the rotating coordinate system and bearing motion; when the rotor rotates at speed ω_j, the center O_j of the rotor journal has a precession extrusion velocity $e\Omega$, where Ω is the instantaneous precession angular velocity, and under the steady synchronous condition, $\Omega = \omega_j$. There is also radial extrusion velocity $\dot{e}$ (e is eccentricity). Furthermore, the stator inner hole can rotate at the angular velocity ω_b, and under such a condition, the trajectory of the rotor center O_j around the stator hole O_b will be unsteady with non-circular precession. Only when e is a constant and $\dot{e} = 0$, the trajectory of O_j has circular precession.

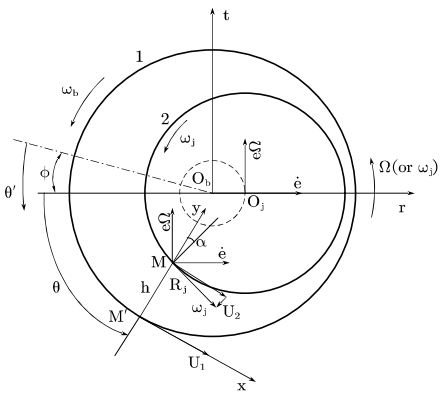

Figure 2. Rotor motion model of CGFS with circular precession in rotating coordinates.

According to the theory of fluid dynamic pressure lubrication, fluid, high rotational speed, and convergence gap are the three basic conditions for forming dynamic pressure lubrication in the sealing gap. Eccentricity and dynamic pressure grooves can form convergence gaps. Therefore, when the rotor rotates at high rotational speed, the gas enters the dynamic pressure groove, and the gas molecules are squeezed, coupled with the kinetic energy of the gas itself, forming a hydrodynamic effect. The fluid dynamic pressure increases, resulting in the formation of a stable gas film in the annular gap.

In the rotating coordinate system (r, t, z) shown in Figure 2, the Reynolds equation of fluid film lubrication for a rotor journal under unsteady precession is established,

$$\frac{1}{R_j^2}\frac{\partial}{\partial\theta}\left(\frac{\rho h^3}{\eta}\frac{\partial p}{\partial\theta}\right)+\frac{\partial}{\partial z}\left(\frac{\rho h^3}{\eta}\frac{\partial p}{\partial z}\right)=6(U_1+U_2)\frac{\partial(\rho h)}{R_j\partial\theta}+12\frac{\partial(\rho h)}{\partial t} \tag{1}$$

where R_j is the external radius of the moving ring (unit: m), θ is the circular coordinate (unit: rad), p is the lubrication film pressure (unit: Pa), h is the film thickness (unit: m), η is the viscosity of lubricating gas (unit: N·s/m^2), z is the axial coordinate (unit: m), U_1 is the translatory velocity of the inner hole of the stator (unit: m/s), U_2 is the translatory velocity of the outer surface of the rotor (unit: m/s).

2.3. Setting of Sealing Structure Parameters

The parameters of the sealing surface mainly include the inner radius of the floating ring R_k, the outer radius of the moving ring R_j, and the length of the sealing ring L. The definitions of each parameter are shown in Figure 3.

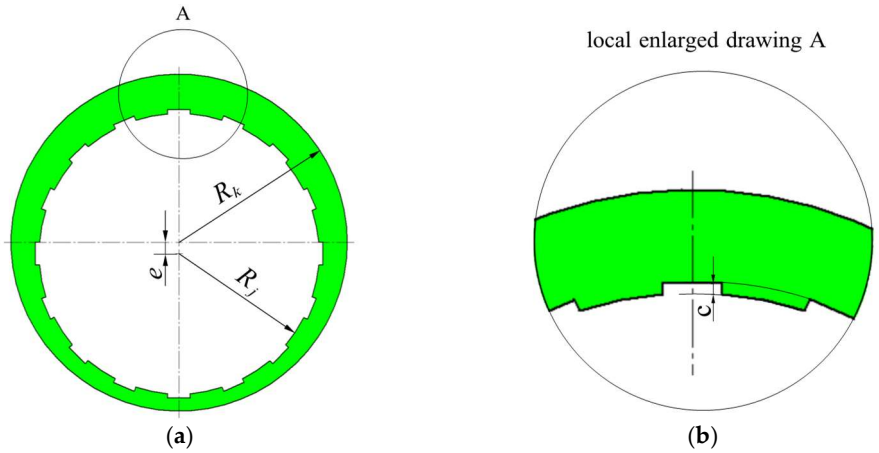

Figure 3. End face of the cylindrical gas film model with the dynamic pressure groove. (**a**) Schematic diagram of gas film model; (**b**) schematic diagram of local enlarged drawing.

The structural parameters of CGFSs include eccentricity e, sealing clearance h, and eccentricity ratio ε. The sealing gap c represents the average gas film thickness formed by the moving ring and the floating ring, and the equation is established.

$$h = R_k - R_j \tag{2}$$

Eccentricity e is the distance between the centerline of the moving ring and the centerline of the floating ring, eccentricity rate ε is a parameter that represents the degree of eccentricity, which can be calculated with Equation (3),

$$\varepsilon = \frac{e}{h} \tag{3}$$

The sealing medium of CGFSs is air, and the sealing medium parameters values are shown in Table 1.

Table 1. Sealing medium parameters of CGFSs (unit in given the bracket).

Parameters	Symbol	Value
Ambient temperature (°C)	T	24
Gas density (kg/m^3)	ρ	1.29
Gas viscosity (Pa·s)	μ	1.79×10^{-5}
Outlet pressure (MPa)	Po	0.1

2.4. Model and Mesh Validation

2.4.1. Gas Film Model

The external radius of the moving ring is 58.4 mm, and the inner radius of the floating ring is 58.41 mm, so the sealing gap is 10 μm.

This study will mainly analyze the flow field characteristics of the no-groove gas film model, T-groove gas film model, and straight-groove gas film model. The groove depth is 10 μm; for the two grooved models, the number of grooves is 16, and the dynamic pressure groove parameters are shown in Figure 4. Three types of gas film models are established based on the control variable method, which is shown in Figure 5.

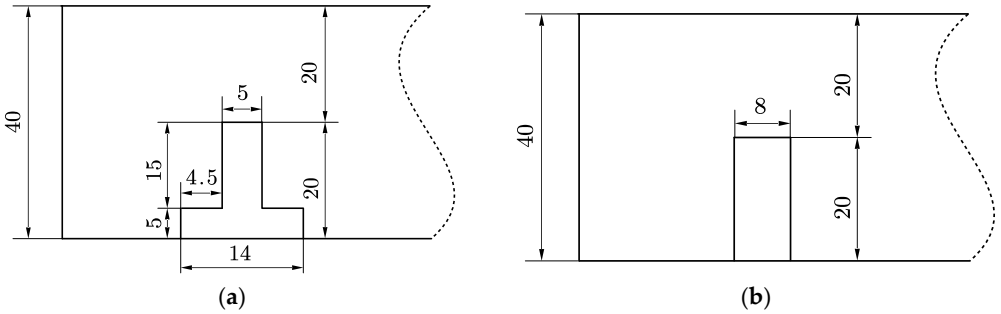

Figure 4. Expansion diagram of two grooved cylindrical gas films. (**a**) T-groove parameters (unit: mm); (**b**) straight groove parameters (unit: mm).

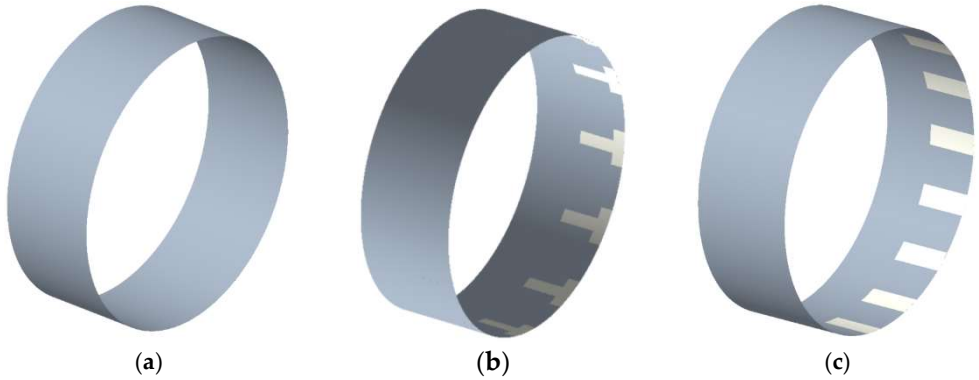

Figure 5. Gas film model. (**a**) No-groove gas film model; (**b**) T-groove gas film model; (**c**) straight groove gas film model.

2.4.2. Mesh Verification

Mesh independence verification is required before simulation to determine whether the mesh quality is acceptable and reduce the time cost. The gas film thickness is a micron, but the fluid domain radius is a millimeter of cylindrical gas film sealing, so it is a cross-scale mesh division. The quality of mesh division affects the accuracy of numerical simulation, so ANSA with high model accuracy is selected as the mesh dividing tool in this study. The hexahedral structure mesh with good orthogonality is used. Figure 6 shows the mesh division diagram of gas film.

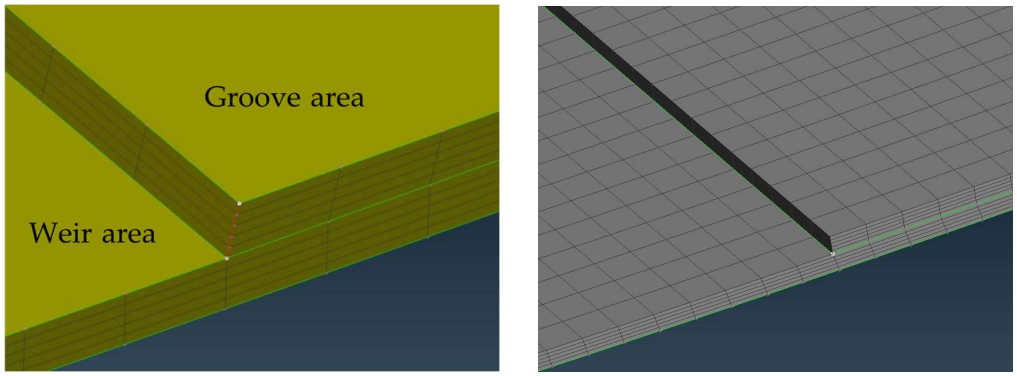

(**a**) (**b**)

Figure 6. Gas film mesh division diagram. (**a**) Mesh layering; (**b**) local volume mesh.

This section verifies the mesh independence using a straight groove cylindrical gas film sealing model; the rotational speed is set at 16,000 rpm, a 10-layer mesh is set up in the groove area, and a 5-layer mesh is set up in the weir area. Select the leakage rate at the pressure outlet as the basis for mesh independence verification. The accuracy of the mesh size and the mesh number is shown in Table 2.

Table 2. Length and mesh number.

Perimeter Length (mm)	0.005	0.01	0.02	0.03	0.04
Mesh number	109,800,000	48,900,000	21,600,000	9,416,250	5,451,300

Figure 7 shows the verification result of mesh independence. When the perimeter length continues to minish from 0.02, the meshes will continue to increase, but the mesh number has little impact on the outlet leakage rate. When the perimeter length is 0.02, the mesh number is 21.6 million, so it can be considered that 21.6 million mesh has reached mesh independence. So, this study will use this perimeter length value for meshing and simulation calculations of various gas film models.

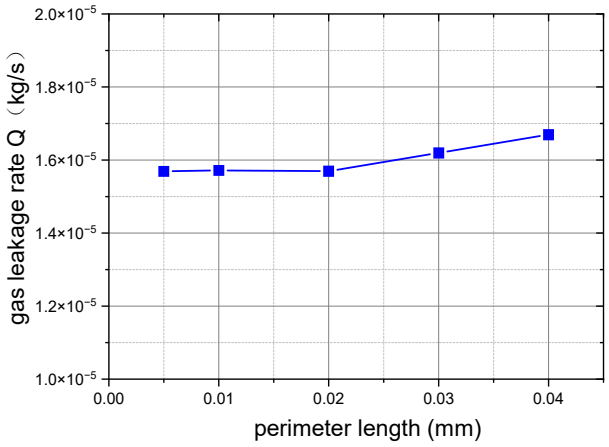

Figure 7. Verification results of gas film mesh independence.

2.5. Basic Assumptions and Boundary Conditions

2.5.1. Basic Assumptions

The operating conditions of cylindrical gas film seal have the following assumptions: First, the gas is an ideal gas (compressible) that is uniform and continuous. Second, the impact of gas inertia force on the flow field is negligible. Third, there is no relative slip between the fluid and the shaft. Last, there is no vibration in the gas film.

2.5.2. Boundary Conditions

To ensure the accuracy of the simulation calculation results, it is necessary to set the model parameters, including fluid flow state, calculation method, and boundary conditions. According to the fluid type and calculation range, set the boundary conditions as follows.

1. The inner ring surface of the fluid domain is the outer ring surface of the moving ring, which simulates the rotation of the shaft using rotational speed conditions, and the interface is a non-slip wall condition.
2. The side with a dynamic pressure groove in the fluid domain is the pressure inlet, and it is the high-pressure side, with a pressure variation range of 0.1 MPa–0.6 MPa.
3. The side without grooves in the fluid domain is the pressure outlet, and it is the low-pressure side, which is connected to the external environment, with a pressure of 0.1 MPa.

3. Integral Formula for Steady-State Characteristics of CGFS

The parameters for studying the performance of CGFSs mainly include the gas film bearing capacity F, friction torque M_f, leakage rate Q, and other parameters.

3.1. Gas Film Buoyancy

When micro-grooves appear on the moving ring of the flexible support CGFSs, the gas film horizontal load F_x can be calculated by Equation (4),

$$F_x = \int_0^L \int_0^{2\pi} \Delta p \cos\theta \cdot R_j d\theta dz \tag{4}$$

The gas film vertical load F_y can be calculated by Equation (5),

$$F_y = \int_0^L \int_0^{2\pi} \Delta pc \sin\theta \cdot R_j d\theta dz \tag{5}$$

where R_j is the outer radius of the moving ring (unit: m), θ is the circumferential angle (unit: degree), P is gas film pressure (unit: Pa), ΔP is differential pressure (unit: Pa), L is the axial length of the sealing gap (unit: m).

The combined force of gas film buoyancy capacity is shown in Equation (6),

$$F_s = \sqrt{{F_x}^2 + {F_y}^2} \tag{6}$$

After dimensionless calculation, we have the Equations (7)–(9),

$$\overline{F_x} = \int_0^L \int_0^{2\pi} (\overline{p} - 1) \cos\theta d\theta d\overline{z} \tag{7}$$

$$\overline{F_y} = \int_0^L \int_0^{2\pi} (\overline{p} - 1) \sin\theta d\theta d\overline{z} \tag{8}$$

$$\overline{F_s} = \sqrt{\overline{F_x}^2 + \overline{F_y}^2} \tag{9}$$

The dimensionless conversion factor for gas film buoyancy is shown in Equation (10),

$$C_F = P_a R_j L \tag{10}$$

where P_a is ambient pressure (unit: Pa), R_j and L are consistent with the above definition.

3.2. Gas Leakage

According to Newton's viscosity law and the assumption of Reynolds Equation [19], through integral calculation, we have the Equations (11) and (12) for the circumferential and axial flow velocity of CGFS, respectively.

$$U = \frac{1}{2R_j\mu}\frac{\partial p}{\partial \theta}(y^2 - yh) + \omega R_j\frac{y}{h} \tag{11}$$

$$V = \frac{1}{2\mu}\frac{\partial p}{\partial z}(y^2 - yh) \tag{12}$$

The volume leakage rate Q can be obtained through integral deduction as shown in Equation (13),

$$Q = \int_0^{2\pi} -\frac{h^3 R_j}{12\mu}\frac{\partial p}{\partial z}d\theta \tag{13}$$

where h is local gas film thickness (unit: m), μ is gas viscosity (unit: N·s/m^2).

The dimensionless conversion factor for leakage rate is shown in Equation (14),

$$C_Q = \frac{m_{mol}\rho_0 P_a C^3 R_i}{24\mu_0 L} \tag{14}$$

where m_{mol} is the molar mass (unit: g/mol), ρ_0 is the gas density (kg/m^3), P_a is the ambient pressure (unit: Pa), C is the average film thickness (unit: m), and μ_0 is the gas ambient viscosity (unit: N·s/m^2).

3.3. Friction Torque

The friction torque M_r is mainly caused by circumferential pressure and viscous shear stress, and the radial friction torque can be obtained using Equation (15),

$$M_r = \int_0^L \int_0^{2\pi} \left(\frac{\partial p}{R_j \partial \theta}\frac{h}{2} + \mu\frac{\omega R_j}{h} \right) R_j \cos\theta d\theta dz \tag{15}$$

The tangential friction torque M_t can be calculated with Equation (16),

$$M_t = \int_0^L \int_0^{2\pi} \left(\frac{\partial p}{R_j \partial \theta}\frac{h}{2} + \mu\frac{\omega R_j}{h} \right) R_j \sin\theta d\theta dz \tag{16}$$

The resultant friction torque M_f is shown in Equation (17),

$$M_f = \sqrt{M_r^2 + M_t^2} = \int_0^L \int_0^{2\pi} \left(-\frac{\partial p}{R_j \partial \theta}\frac{h}{2} + \mu\frac{\omega R_j}{h} \right) R_j^2 d\theta dz \tag{17}$$

where ω is the shaft angular velocity (unit: rad/s), h is film thickness (unit: m), R_j is the outer radius of the moving ring (unit: m), θ is the circumferential angle (unit: degree), p is the gas film pressure (unit: Pa), and μ is gas viscosity (unit: N·s/m^2).

Dimensionless friction torque $\overline{M_f}$ is shown in Equation (18), and the friction torque conversion coefficient C_M is shown in Equation (19),

$$\overline{M_f} = \sqrt{\overline{M_r^2} + \overline{M_t^2}} \tag{18}$$

$$C_M = p_0 C L R_j \tag{19}$$

3.4. Gas Film Stiffness

Gas film stiffness is the ratio between the increment of film buoyancy and the increment of film thickness. It reflects the gas film-bearing capacity. The stiffness formula is shown in Equation (20):

$$K_{zz} = -\left.\frac{\partial F_z}{\partial h}\right|_{h0} = -\frac{F_2 - F_1}{h_2 - h_1} \tag{20}$$

where, F_1 is the film buoyancy when the film thickness is h_1 (N), F_2 is the film buoyancy when the film thickness is h_2 (N), h_1 is the average film thickness at the start point (m), and h_2 is the average film thickness at the endpoint (m).

4. Experiment of CGFS

During the process of the CGFS experiment, changing parameters and values can lead to different experimental phenomena and results. Based on the conclusions of experiments, numerical calculation methods and models can be optimized to reveal the impact mechanism of simulation results and phenomena accurately. This section carries out the leakage measurement experiment for CGFSs, verifies the numerical simulation research results, and provides guidance for the selection of grid models and calculation models.

4.1. Experimental Principle

This section takes the leakage rate as the target parameter to study the variety rule of leakage with rotational speed. Upon comparing the results of experiments and numerical analyses, reasonably grid models and mathematical models were selected to ensure the correctness of numerical analysis calculation results. The rotor rotational speed increases from 3600 rpm to 19,800 rpm. The inlet pressures are 0.3 MPa, 0.4 MPa, 0.5 MPa, and 0.6 MPa, respectively, and the outlet pressure is 0.1 MPa, so the pressure differentials between inlet and outlet are 0.2 MPa, 0.3 MPa, 0.4 MPa, and 0.5 MPa, respectively.

The CGFS experiment system includes a laser marking machine, a gas supply system, a power system, a sealing test rig, a state detection monitors system, a leakage measurement system, and a three-dimensional topography measuring instrument. The composition of the experiment system is shown in Figure 8. A laser marking machine is used to provide dynamic pressure grooves on the surface of moving rings. The gas supply system provides compressed gas and sends the gas into the sealing cavity through the pipeline. The power system provides power for the rotor of the sealing test rig. The three-dimensional morphology measuring instrument detects the quality of the dynamic pressure grooves and the surface roughness of the sealing component. The leakage measurement system measures the leakage at the outlet. The state detection system monitors real-time status parameters during the experiment, such as rotor rotational speed, inlet pressure, etc.

4.2. Design of Experimental Plan

The experiment used both no-groove and double-row groove moving rings, and the material of the moving rings is SiC, with an outer diameter of 49.96 mm. The floating ring material is graphite M254 with an inner diameter of 50 mm. The sealing gap is 20 μm. The floating ring thickness is 13 mm. In this section, the rotational speed is 3600 rpm to 19,800 rpm. The inlet pressures are set to 0.3 MPa, 0.4 MPa, 0.5 MPa, and 0.6 MPa, respectively. The outlet pressure is 0.1 MPa, so the pressure differential is 0.2 MPa to 0.5 MPa. The inlet temperature is 24 °C, and the outlet temperature is 24 °C. The gas viscosity is 1.79×10^{-5} Pa·s.

The experiment used a double-row grooves moving ring, the gas inlet located in the middle of the moving ring, and the gas outlet located on both end faces of the moving ring. This symmetrical dual runway design can reduce the system error caused by the structure of the gas path during the experiment; however, the leakage measured in the experiment is the average value of the double outlets, which ensures that the experiment and numerical calculation have the same operating conditions, and the results are comparable. The dynamic pressure groove structural parameters in the experiment are shown in Table 3.

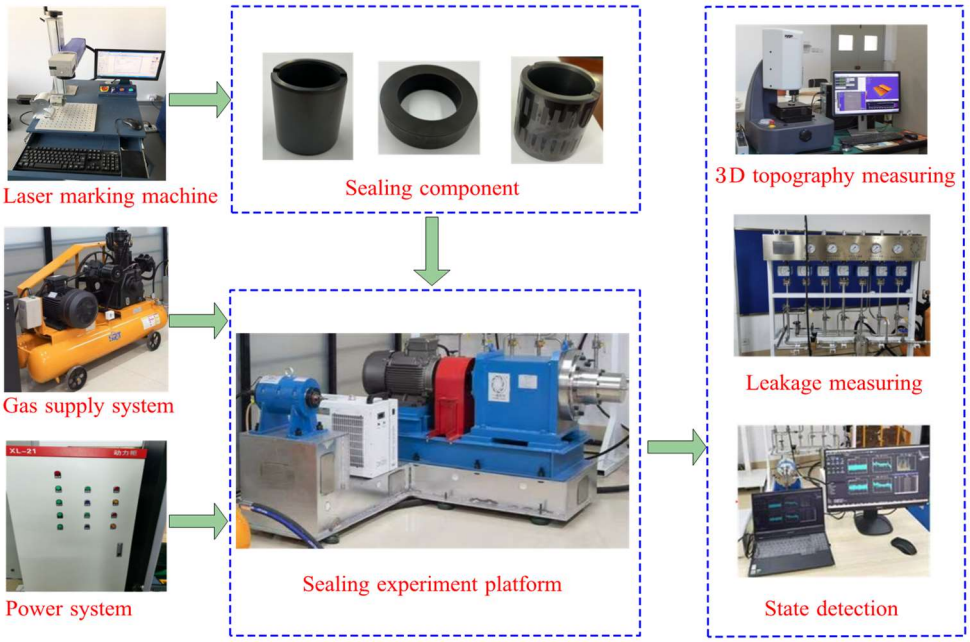

Figure 8. Connection diagram of cylindrical gas film seal experiment system.

Table 3. Groove parameters of double-row grooves.

Groove Number	Groove Depth	Groove Length	Groove Width
16	10 μm	15 mm	5 mm

4.3. Analysis of Experiment Results

Figure 9 shows the leakage rates of two types of grooves under different pressure differential in experiments. In Figure 9a, when the pressure differential is 0.2 MPa and 0.3 MPa, the leakage rate of the no-groove gas film changes similarly, and it decreases with an increase in rotational speed. When the pressure differential is 0.4 MPa and 0.5 MPa, the leakage rates decrease with an increase in rotational speed. When the rotational speed exceeds 15,000 rpm, the leakage rate gradually stabilizes. In Figure 9b, when the pressure differential is 0.2 MPa, 0.3 MPa, and 0.4 MPa, the leakage rate slowly decreases with an increase in speed for the two double-row grooves. However, when the pressure differential is 0.5 MPa, the leakage rate rapidly decreases with an increase in rotational speed. Overall, the leakage rate of both grooves decreases with an increase in rotational speed. The larger the pressure differential, the greater the leakage.

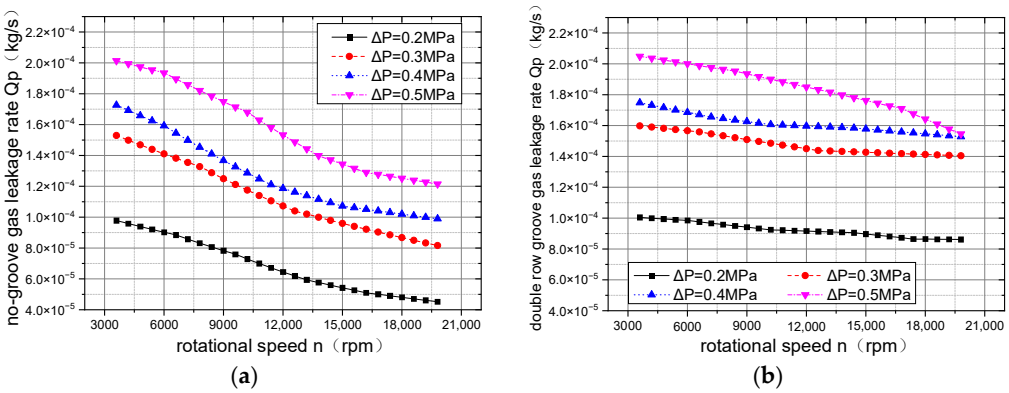

Figure 9. Gas leakage rate at different pressure differentials. (**a**) No-groove moving ring; (**b**) double-row grooves moving ring.

5. Numerical Calculation and Verification of Leakage

5.1. Comparative Analysis of Calculation Results

According to calculations, when the rotational speed is 100,000 rpm, the Reynolds number is 357. Therefore, the gas flow state is laminar within the rotational speed range in this study. To further verify the flow state and select a computational model, three calculation models (LAMINAR model, k-ε model, and SAS model) are selected in the simulation software. At the beginning of the research study, gas film mesh was divided into 1–10 layers; through preliminary comparison with the experimental results, the number of mesh layers most consistent with the experimental results of the three mathematical models under two pressure differentials was obtained, as shown in Figure 9.

Figure 10 shows the leakage rate calculated using different mathematical models for the no-grooved dynamic ring gas film at pressure differentials of 0.2 MPa and 0.3 MPa. The leakage rate computed using a 5-layer grid and a LAMINAR calculation model is closest to the experimental value in Figure 5. For the standard k-ε model, although the model has fewer layers and lower computational costs, there is a significant difference between the numerical value and experimental data. The calculation results of the SAS model are consistent with the experimental value at speeds below 12,000 rpm; when the speed exceeds 12,000 rpm, the changing trend of leakage rate is opposite to the experimental value. Therefore, the SAS model is unsuitable for numerical analysis under this operating condition.

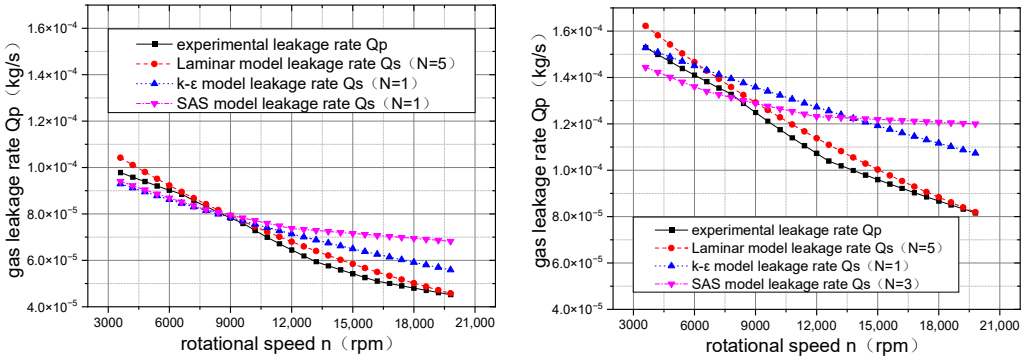

Figure 10. Comparative analysis of leakage rate. (**a**) Δp = 0.2 MPa; (**b**) Δp = 0.3 MPa.

5.2. Error Analysis

Figure 11 is the error bar diagram of the simulation value and experimental value of the leakage when using the LAMINAR calculation model and no-groove moving ring. The black curve in Figure 6 is the experimental leakage rate, and the yellow ribbon is the fluctuation area of the simulation leakage rate. Based on Figure 11a, we can see that when the pressure differential is 0.2 MPa, the maximum leakage rate error occurs at a speed of 15,000 rpm, with a relative error of 7.7%. We also can see that when the pressure differential is 0.3 MPa, the maximum error of leakage occurs at a speed of 12,600 rpm in Figure 11 b, and the relative error is 6.7%. As the speed increases, the relative error first decreases from large to small but then increases from small to large and finally begins to fall, showing a fluctuating state. The relative error of leakage rates under two different pressure differentials is within 7%, which meets the accuracy requirements of numerical calculation. The macro and micro characteristics of gas film structure size, the vibration of the experimental system, and the neglect of equipment installation errors and deformation errors during simulation analysis are the main reasons for the errors.

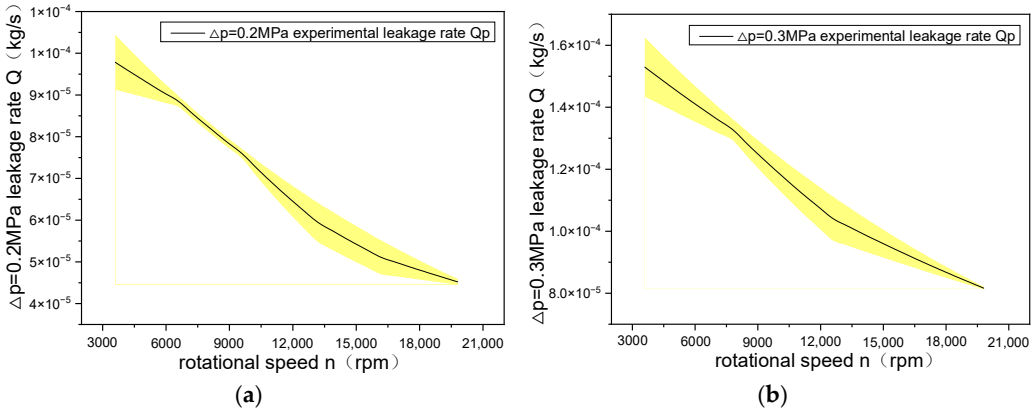

Figure 11. Leakage rate error bar diagram. (**a**) Δp = 0.2 MPa; (**b**) Δp = 0.3 MPa.

6. Formation Mechanism of Dynamic Pressure in Flow Field

The influencing factors of the gas film characteristics of flexible support CGFS include gas flow state, gas physical characteristics, deformation of floating rings and wave foils, etc. This section studies the dynamic characteristics of gas film in micro gap flow fields and the impact of the axial pressure distribution, gas film velocity, and operating parameters on the gas film sealing performance.

The differential pressure flow in the micro gap of the CGFS flows to the outlet and the shear flow along the circumferential direction with the rotation of the rotor. This section studies the distribution of fluid pressure in annular clearances under different rotational speeds and pressure differential. We also study the impacts of rotational speeds and pressure differential on fluid flow states.

6.1. The Impact of Rotational Speed on the Pressure Distribution in the Groove Area

To study the characteristics of the gap flow field at different rotational speeds, we set the inlet pressure at 0.3 MPa and the outlet pressure at 0.1 MPa. Therefore, the pressure differential is 0.2 MPa. The rotational speeds are set to 10,000 rpm, 20,000 rpm, and 30,000 rpm, respectively. Figure 12 shows the distribution of the straight groove cylindrical film pressure at different rotational speeds. The arrow in Figure 12a shows the rotation direction of the moving ring. The gas pressure in the annular gap flow field increases with an increase in rotational speed, and the high-pressure areas are concentrated in the transition zone of the groove and weir along the direction downstream. This is because the higher the rotational speed, the more shear flow caused by the rotor rotation. When the fluid in the annular gap flows along the circumferential direction, the hydrodynamic effects are generated due to the blocking of the weir area, forming a high-pressure region.

Figure 13 shows the distribution of the T-groove cylindrical film pressure at different rotational speeds. The arrow in Figure 13a shows the rotation direction of the moving ring. The fluid change rule in the T-groove annular gap is similar to the straight groove. The high-pressure area of the T-groove is mainly concentrated in the transition area between the wing groove and the weir area. This is because as the speed increases, the shear flow quickly moves to the weir area and thus forms a high-pressure area under the hydrodynamic effects. Upon comparing with Figure 11, we can see that at the same rotational speed, the pressure in the T-groove is greater than that in the straight groove, but the high-pressure area in the T-groove is smaller than that in the straight groove. This is because the blocking effect of the weir area at the root of the T-groove wing groove affects the expansion of the high-pressure area.

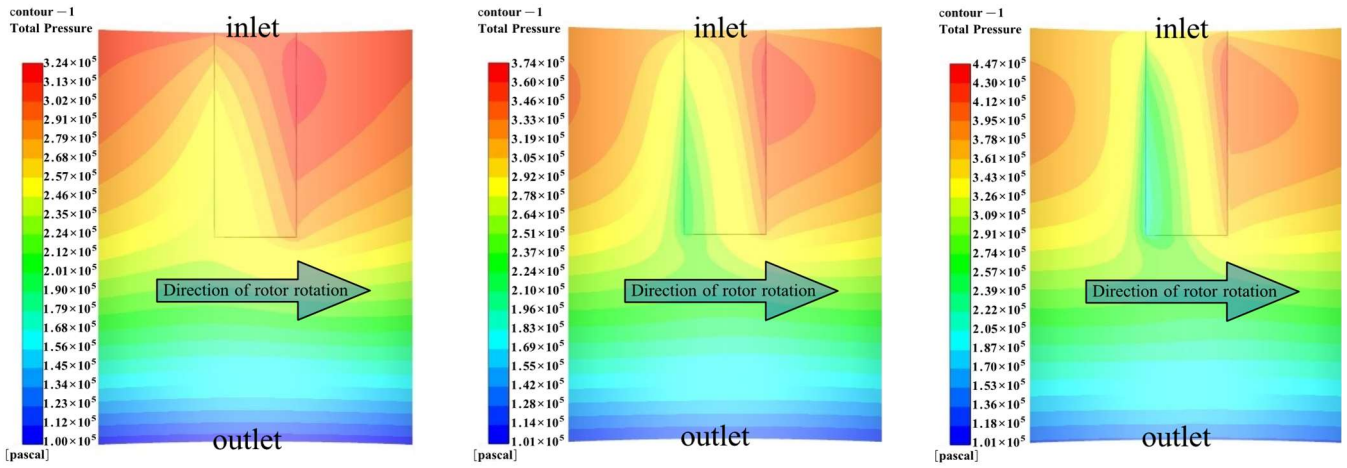

Figure 12. Effect of rotational speed on film hydrostatic pressure in the straight groove. (**a**) 10,000 rpm; (**b**) 20,000 rpm; (**c**) 30,000 rpm.

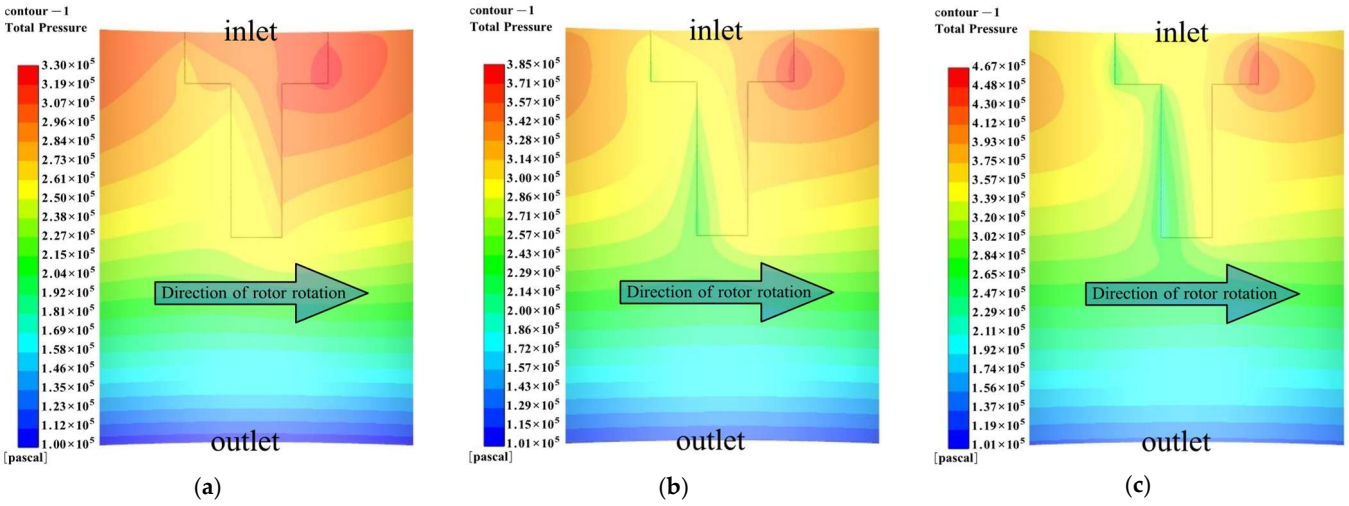

Figure 13. Effect of rotational speed on film hydrostatic pressure in T-groove. (**a**) 10,000 rpm; (**b**) 20,000 rpm; (**c**) 30,000 rpm.

6.2. The Impact of Differential Pressure on the Pressure Distribution in the Groove Area

To study the characteristics of the gap flow field at different pressures, we set the rotational speed at 8000 rpm, the outlet pressure at 0.1 MPa, and the pressure differentials at 0.2 MPa, 0.4 MPa, and 0.6 MPa, respectively. Figure 14 shows the distribution of the straight groove cylindrical film pressure at different pressure differentials. The arrow in Figure 14a shows the rotation direction of the moving ring. As shown in Figure 14, the larger the pressure differential, the larger the area of the high-pressure zone.

Figure 15 shows the distribution of the T-groove gas film pressure at different differential pressures. The arrow in Figure 15a shows the rotation direction of the moving ring. The pressure change rule in Figure 15 is similar to the situation in Figure 14. This is because as the pressure differential increases, there is more pressure differential flow along the axis direction, and the fluid in the gap varies linearly along the axial direction. Therefore, it is difficult for the circumferential weir area to generate strong hydrodynamic effects, while the axial dam area can form strong hydrodynamic effects.

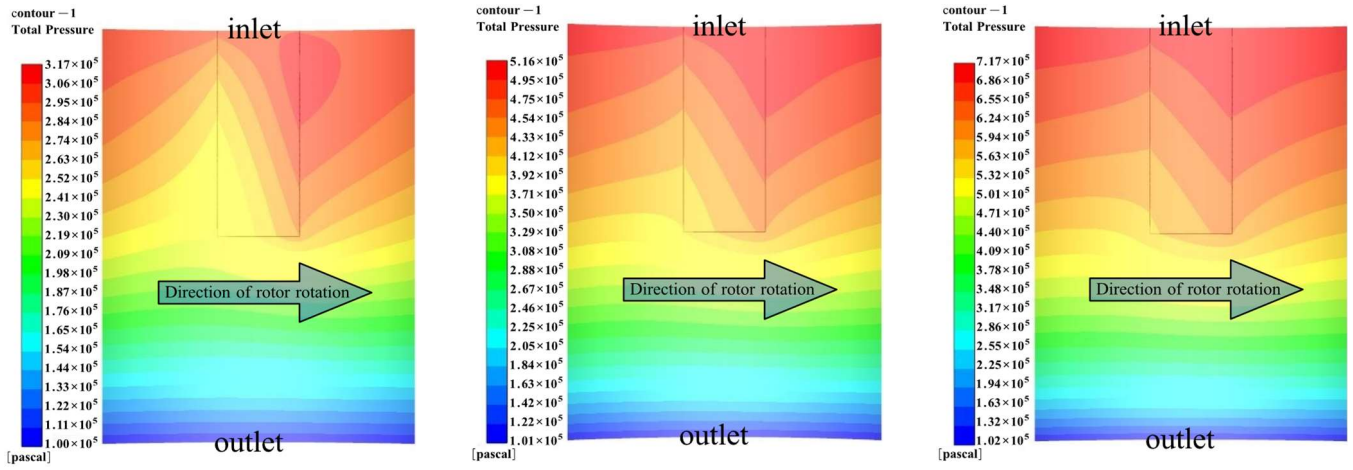

Figure 14. Effect of pressure differential on film hydrostatic pressure in a straight groove. (**a**) 0.2 MPa; (**b**) 0.4 MPa; (**c**) 0.6 MPa.

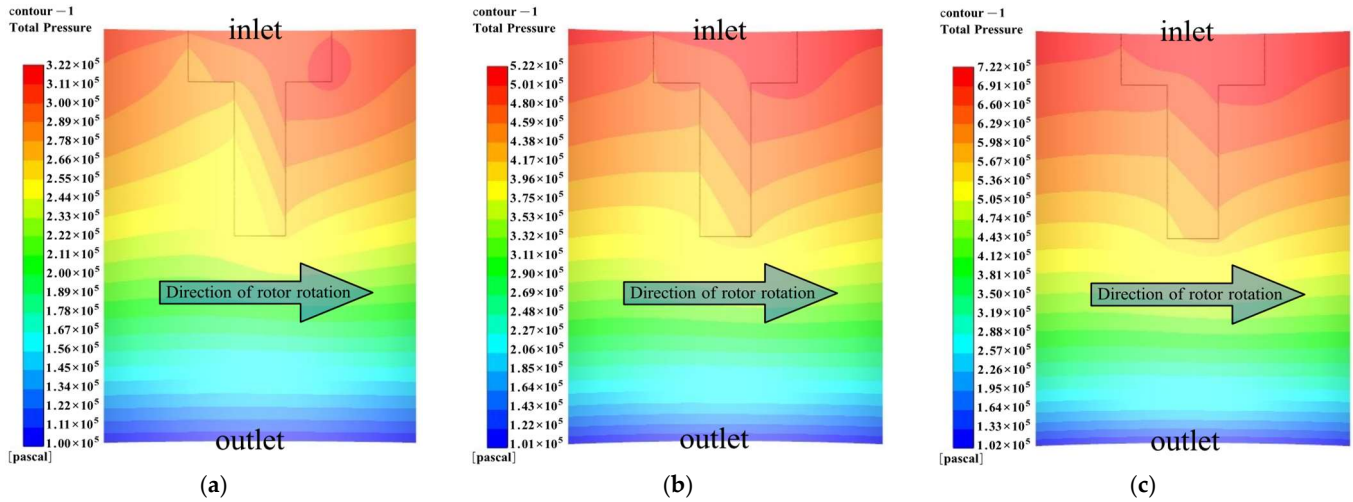

Figure 15. Effect of pressure differential on film hydrostatic pressure in T-groove. (**a**) 0.2 MPa; (**b**) 0.4 MPa; (**c**) 0.6 MPa.

According to the simulation calculation results and the circular annular gas flow theory, it is known that rotational speed is the main reason for forming shear flow, and the pressure gradient between the inlet and outlet is the crucial factor in forming differential pressure flow. The gas flow between gaps results from the combined action of these two flows. The maximum fluid pressure occurs at the intersection position of the groove and the weir of the dynamic pressure groove. The length and direction of the boundary between the groove and weir are the crucial factors affecting the flow field pressure distribution. From the overall pressure distribution and values, the straight groove is superior to the T-groove.

7. Aerodynamic Characteristics and Sealing Performance of Gas Film

This section studies the influence of operating parameters on the aerodynamic characteristics and seal ability of no-groove, straight grooves, and T-groove gas film and explores the relation between working parameters and aerodynamic characteristics and sealing performance.

7.1. The Impact of Rotational Speed on Flow Field Characteristics

The change rule of gas film buoyancy and stiffness with rotational speed is shown in Figure 16, and the result shows that the gas film buoyancy of both groove models significantly increases when the rotational speed increases; this is because high rotational speed can bring more gas into the micro convergence gap, which increases the internal pressure of the gap and enhances the hydrodynamic effects. We can see that the gas film buoyancy generated by the straight groove is higher than the T-grooves. Due to the large inlet of the T-groove, when a large amount of gas is pumped into the gap, the gas pressure increases at the wing groove first, but the pressure is small. However, the channel of the straight groove is long, and when the gas moves to the bottom of the groove, the pressure increases due to the blockage of the dam area, and the gas pressure rapidly increases, so the gas film buoyancy increases, which is significantly higher than the T-groove. The gas film stiffness reflects the ability of the gas to resist deformation and maintain stability. As the rotational speed increases, the gas film-bearing capacity increases. So, the ability of the gas to resist external interference increases, and the gas film stiffness of the three models grows with an increase in rotational speed.

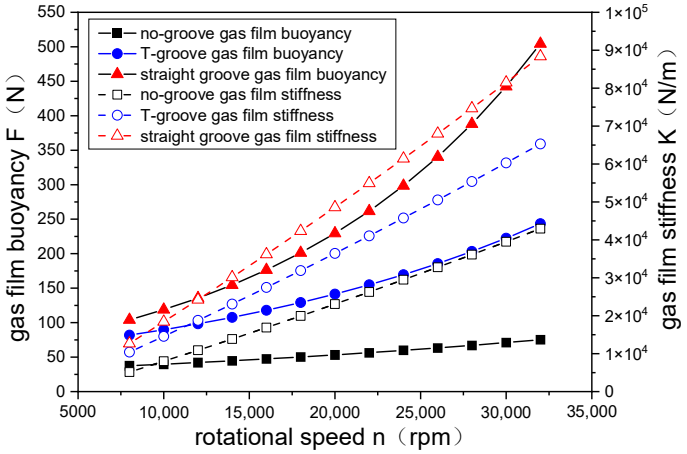

Figure 16. The change law of gas film buoyancy and stiffness with rotational speed.

Figure 17 shows the change curve of gas leakage rate and gas friction torque with rotational speed for three types of grooves. The inlet pressure is 0.3 MPa, the outlet pressure is 0.1 MPa, and the pressure differential is 0.2 MPa. As the rotational speed increases, the leakage rate of the three types of gas film decreases with an increase in rotational speed. When the rotational speed increased from 8000 rpm to 32,000 rpm, the leakage rate of the straight groove decreased by about 50%, the leakage rate of the T-groove decreased by 45%, and the leakage rate of the no-groove gas film decreased by only 21%. It can also be seen that the leakage rate of the no-groove gas film was greater than that of the other two types of gas film. This indicates that the dynamic pressure groove can effectively reduce leakage rate; when the gas flows to the bottom of the dynamic pressure groove, it is blocked by the weir and dam, resulting in a significant reduction in axial leakage rate. The leakage rate of the grooved gas film is significantly smaller than that of the no-groove film. When the gas rotates at high speed, the macro-gas friction force is generated because of the Newtonian viscous shear force and the viscous force. However, due to the tiny rotational radius of the gas and the small gas viscosity, the friction torque is very low. We can see that with an increase in rotational speed, the friction torque of gas films increases, as shown in Figure 17. It indicates that the higher the rotational speed, the greater the resistance between gas molecules in the micro gap. The friction torque growth rate of the straight-grooved model is the highest, followed by the T-groove and no-groove models.

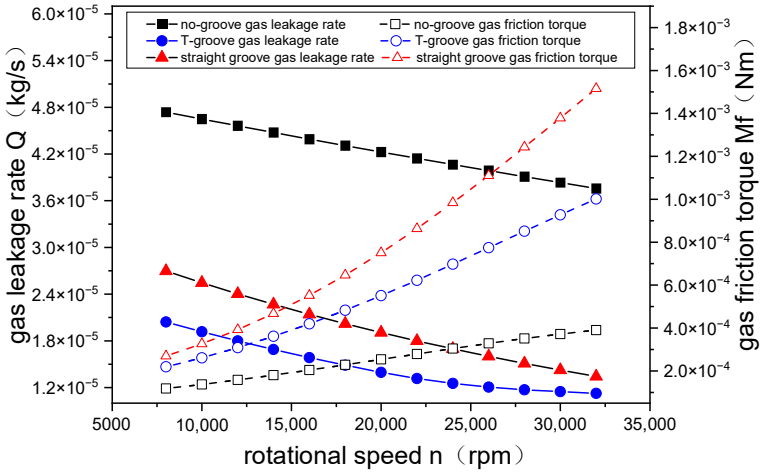

Figure 17. The change law of gas film leakage rate and gas friction torque with rotational speed.

Based on Figures 16 and 17, we can see that the gas buoyancy, gas film stiffness, and friction torque of the three types of grooves increase with rotational speed increases, while the leakage rate shows a decreasing trend. This indicates that as the rotational speed increases, the movement of gas molecules in the micro gap flow field will intensify. The high-speed flowing gas produces strong hydrodynamic effects under the action of the circumferential convergence gap and dynamic pressure groove, resulting in increases in gas film buoyancy and stiffness, thereby improving the sealing characteristics and reducing leakage rate. Therefore, under high rotational speed conditions, the aerodynamic characteristics and sealability of the straight groove are superior to the other two models.

7.2. The Impact of Differential Pressure on Flow Field Characteristics

To investigate the impact of differential pressure on flow field characteristics, we set the differential pressure to vary from 0.1 MPa to 1.0 MPa, with a pressure differential increment of 0.1 MPa, while keeping other parameters unchanged.

Figure 18 shows the variation in pressure increment with differential pressures for three types of grooves. The pressure increment is the difference between the gas film pressure and the pressure differential. When the pressure increment is used to analyze the impact of the pressure differential on the gas film pressure, the numerical misdirection caused by the pressure differential itself can be eliminated. For the T-groove CGFS, the pressure increment slowdown when the differential pressure is 0.1 MPa, the pressure increment of gas is 65,633 Pa, and when the differential pressure is 1.0 MPa, the pressure increment of gas is 45,229 Pa. The pressure increment has decreased by 31%. For the CGFSs with a straight groove, when the differential pressure increases from 0.1 MPa to 1.0 MPa, the gas pressure increment decreases by 53%. Compared with the T-groove, the gas film pressure increment of the straight groove decreases more rapidly. The gas film pressure increment of the no-groove model is similar to that of the straight groove. This indicates that for CGFSs, the enhancement effect of differential pressure on fluid dynamic pressure weakens with an increase in pressure differential.

Figure 19 shows the change law of gas buoyancy and gas film stiffness with pressure differential. The gas buoyancy of the three types of grooves all increase with an increase in pressure differential. The gas film buoyancy of the straight groove remains the highest throughout the process of pressure differential increase, followed by the T-groove, and the smallest is the no-groove model. Compared with the T-groove, the flow channel of the straight groove is single. When the gas pump enters the sealing gap, the axial pressure forces the gas film to flow along the axial direction to the bottom of the groove, and after the dam blocks the gas, the gas film pressure rapidly increases and forms strong hydrodynamic effects in the groove. The T-groove has two dam zones, and when gas flows into the T-groove along the axial direction, it needs to pass through the blocking

effect of the dam area at the bottom of the wing groove and the bottom of the web groove. Therefore, two high-pressure zones are formed at the bottom of the two grooves, but the value is smaller than the straight groove. Due to the lack of converging grooves in the axial direction, the no-groove model can only rely on eccentric gaps to generate dynamic pressure. Therefore, the hydrodynamic influence is weak, and the gas buoyancy of the no-groove model is lower than the other two grooved models. The gas film stiffness of the three grooved models grows with the rotational speed increases. The film stiffness of the straight groove always remains the highest during the change in pressure differential, followed by the T-groove, and the no-groove models with the lowest film stiffness.

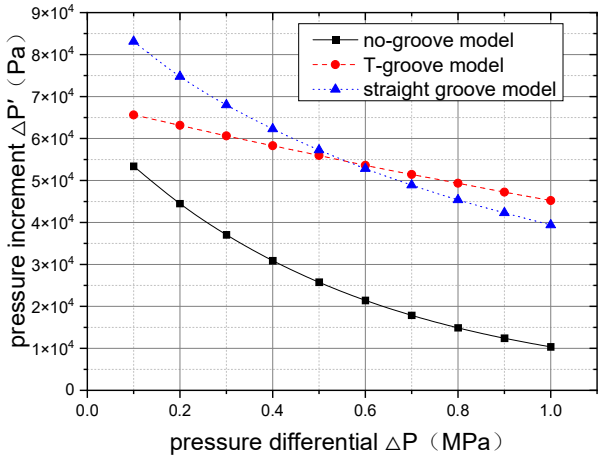

Figure 18. Curve of film pressure increment with pressure differential.

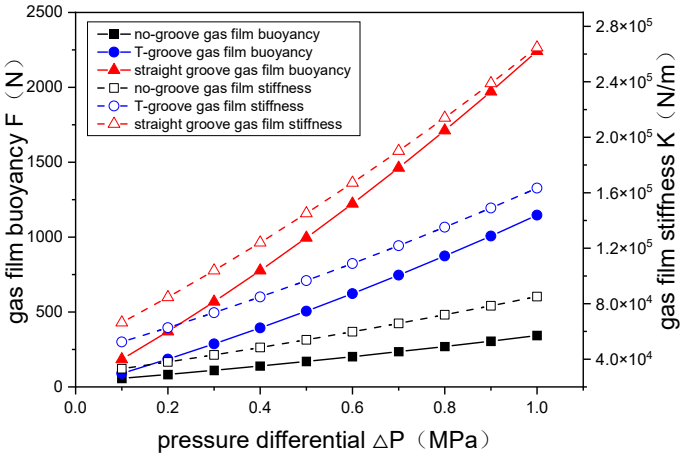

Figure 19. The change law of gas film buoyancy and stiffness with pressure differential.

Figure 20 shows the change curve of gas leakage rate and gas film friction torque with pressure differential. The rotational speed is set to 28,000 rpm. The gas leakage rate of the three grooved models increases with an increase in pressure differential. The gas leakage rate of the no-groove remains the highest during the process, while the gas leakage rate of the two grooved models is low, and the change trend is similar. The gas leakage rate of the straight groove is greater than that of the T-groove because as the pressure differential increases, the amount of gas flowing into the gap rises, and the gas flow direction mainly flows along the axial line, resulting in an increase in leakage rate. The gas leakage rate of the two grooved models is significantly lower than that of the no-groove model, with the two-stage dam of the T-groove having a noticeable effect on reducing gas leakage. The friction torque of the three types of grooves increases with an increase in pressure differential; the straight groove growth rate is the highest, followed by the T-groove, while

the growth of the no-groove gas film friction torque is slow. Due to the low viscosity of gas, the friction torque of gas is small.

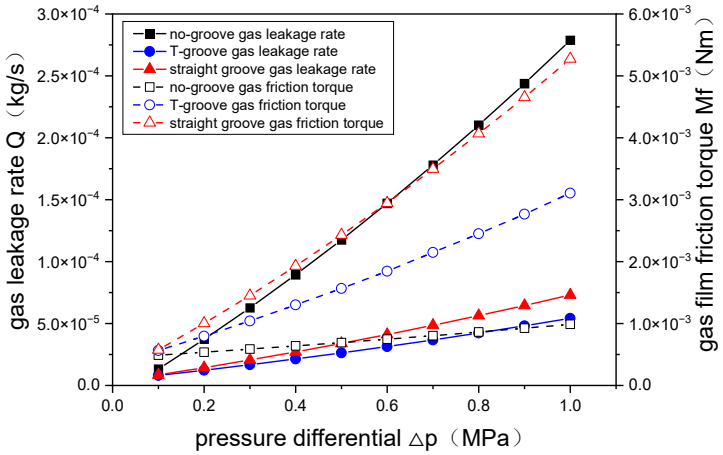

Figure 20. Change law of gas leakage rate and gas film friction torque with pressure differential.

In summary, when the pressure differential increases, the gas buoyancy, gas film stiffness, and friction torque of the three types of grooves all show an upward trend; the values of the straight groove model are the highest during the pressure differential variation process. The gas leakage rates of the three types of grooves also increase with the pressure differential increases, and the leakage rate of the no-groove gas film is greater than those of the other two grooved models. It indicates that the larger the differential pressure, the greater the hydrodynamic effects and the higher the gas buoyancy and gas stability. However, the high pressure at the inlet creates a strong differential pressure flow in the gap, resulting in a large amount of end leakage at the outlet, which increases the overall leakage rate. By comparison, the straight groove has good aerodynamic characteristics and sealing characteristics under a high-pressure differential.

7.3. The Impact of Film Thickness on Flow Field Characteristics

To investigate the impact of film thickness on flow field characteristics, we set the inlet pressure to 0.3 MPa, the outlet pressure to 0.1 MPa, the rotational speed to 2800 rpm, the eccentricity rate to 0.4, and the variation range of gas film thickness is 10 μm~90 μm.

Figure 21 shows the change curve of the gas film buoyancy and gas film stiffness with the film thickness. We can see that as the film thickness increases, the gas film buoyancy of the three types of grooves decreases. As the film thickness increases, the gas shear rate decreases, and the hydrodynamic effect decreases, resulting in a decrease in the gas film-bearing capacity. Through further observation, we can observe that when the gas film thickness exceeds 90 μm, the hydrodynamic action in the sealing gap of the three types of models almost disappears. We can also see that the film stiffness of the three types of grooves decreases as the film thickness increases, while the no-groove film stiffness decreases the fastest, and the film stiffness of the straight groove is similar to the T-groove. When the film thickness increases, the T-groove two-stage weir area plays a positive role in slowing down the film stiffness and improving film stability.

Figure 22 shows the variation curve of gas leakage rate and gas film friction torque with film thickness. We can see that the leakage rate of the three film models increases with an increase in film thickness, and the no-groove gas film increases approximately linearly. The gas leakage rate of straight grooves is slightly higher than T-grooves because when the film thickness increases, the gas gap expands, and the hydrodynamic effects decrease or even disappear, resulting in a flow rate increase in the leakage. The friction torque of different grooves decreases as the film thickness increases. The thickness of the gas film varies from 10 μm to 60 μm. The decrease rate of friction torque is the highest, with a 64% decrease in friction torque for the no-groove gas film. When the film thickness exceeds

60 μm, the decrease rate of friction torque gradually slows because when the film thickness increases, the flow channel expands, the hydrodynamic effects decrease, and the friction force between gas molecules decreases, resulting in a decrease in friction torque.

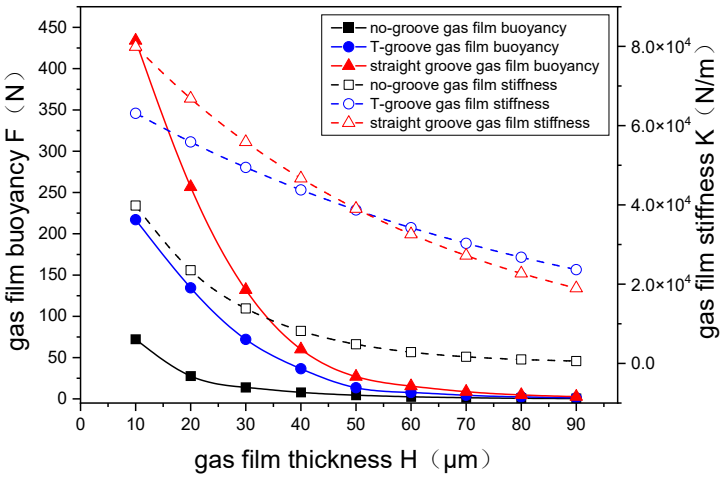

Figure 21. The change law of gas film buoyancy and stiffness with gas film thickness.

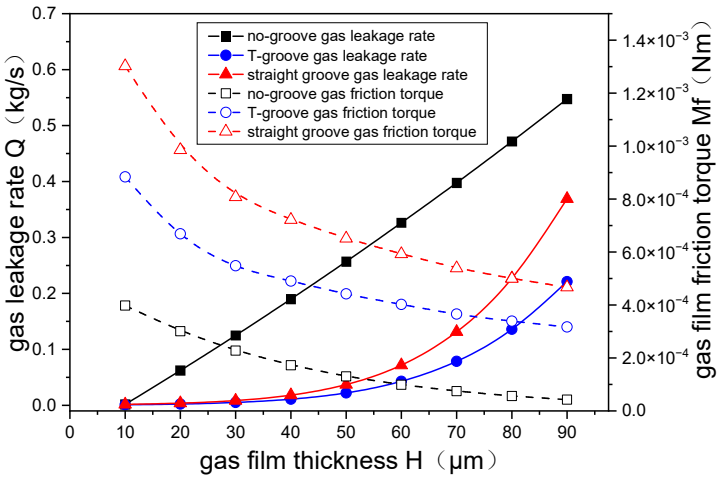

Figure 22. The change law of gas leakage rate and gas film friction torque with gas film thickness.

In summary, when the film thickness increases, the gas buoyancy, gas film stiffness, and friction torque of the three types of grooves show a decreasing trend while the gas leakage rate increases. This indicates that micro-gap is the essential condition for generating hydrodynamic effects. When the gas film thickness increases, the hydrodynamic effects disappear, the aerodynamic characteristics and sealability of the gas film also decrease, and the sealing stability will be greatly affected.

7.4. The Impact of Eccentricity Rate on Flow Field Characteristics

To investigate the impact of eccentricity rate on flow field characteristics, we set the inlet pressure at 0.3 MPa, the outlet pressure at 0.1 MPa, the rotational speed at 2800 rpm, the film thickness at 10 μm, and the change range of eccentricity rate is 0.1~0.9. Figure 23 shows the variation curve of the gas buoyancy and gas film stiffness with eccentricity rate. As the eccentricity rate increases, the gas buoyancy of the straight groove and T-groove increases rapidly, while the buoyancy of the no-groove model slowly increases. The eccentricity rate has a significant impact on the gas buoyancy because the larger the eccentricity rate, the smaller the minimum gap, and the greater the overall hydrodynamic effects formed by the dynamic pressure grooves and eccentric wedge. As the eccentricity rate increases, the

difference in gas buoyancy between the two grooved gas films becomes more apparent, and the gas buoyancy of the straight groove is greater than that of the T-groove. We can also see that the film stiffness of the three models increases with an increase in eccentricity rate. The film stiffness of the no-groove increases and is smaller than that of the other two models since the film stiffness of the T-groove and the straight groove increases rapidly. As the eccentricity rate increases, the two-stage weir area of the T-groove has an obvious effect on improving the hydrodynamic action, greatly improving gas stability.

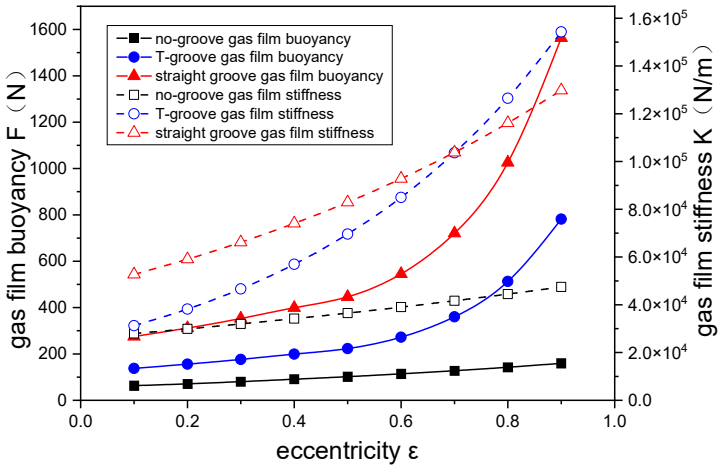

Figure 23. The change law of gas film buoyancy and stiffness with eccentricity rate.

Figure 24 shows the change curve of gas leakage rate and gas film friction torque with eccentricity rate. As the eccentricity rate increases, the leakage rates of all three models show an upward trend. The gas leakage rate of the no-groove model is faster than those of the other two grooved models. The main reason is that as the eccentricity rate increases, the distribution of the gas becomes more non-uniform, and the gas flow at the position with the maximum gas film thickness will sharply increase, resulting in a significant increase in the overall leakage. The friction torques of all three groove models increase with an increase in eccentricity rate. This is because as the eccentricity increases, although the friction torque at the small film thickness increases, the friction torque at the largest film thickness decreases, and the overall friction torque shows an upward trend.

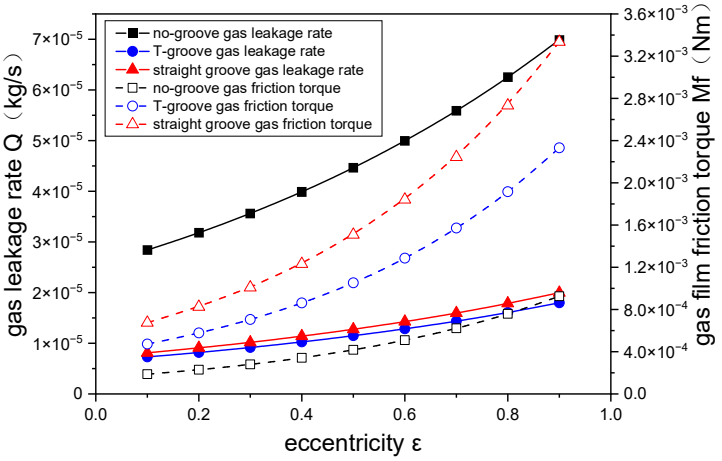

Figure 24. The change law of gas leakage rate and gas film friction torque with eccentricity rate.

In summary, as the eccentricity rate increases, the gas buoyancy, gas film stiffness, friction torque, and gas leakage rate of the three groove models all show an upward trend. As the eccentricity rate increases, the minimum film thickness decreases, the hydrodynamic ef-

fects increase, the gas buoyancy increases and the gas film stability also increases. However, as the eccentricity rate increases, the maximum gas film thickness also increases, and the leakage rate also increases. Upon comparing the characteristic curves of the three gas film models, we found that the straight groove has relatively better aerodynamic characteristics and sealing characteristics at different eccentricities.

8. Conclusions

In this study, a CGFS test rig was first used to conduct physical tests under four different pressure differentials, and the results were tested and analyzed. This study investigated the gas leakage rate at Δp = 0.2 MPa and Δp = 0.3 MPa, respectively, and compared and analyzed the experimental and computational results. Finally, this study analyzed the flow field characteristics of the three groove models' micro gaps based on the optimized computational model and the cross-scale gas film grid model. The main conclusions are as follows:

(1) The physical test results show that the leakage rate under all four pressure differentials decreases with an increase in rotational speed. The larger the pressure differential, the greater the overall leakage of the CGFS. This indicates that the higher the rotational speed, the smaller the eccentricity rate and the more uniform the gap gas film thickness, resulting in a smaller leakage rate. The dynamic pressure groove will increase the average gas film thickness, and compared with the no-groove model, the leakage rate of the grooved model will slightly increase.

(2) Upon computing the gas leakage rate of three chosen models and five different gas film grid accuracies, we found that the accuracy of the LAMINAR model computed result is better than the standard k-ε models and SAS models. When using the LAMINAR model and the 5-layer gas film model, the calculated leakage rate is highly consistent with physical test data.

(3) The buoyancy, film stiffness, and friction torque of the three groove models increase with the rotational speed increases, pressure differential, and eccentricity rate. When the film thickness increases, the gas buoyancy, gas film stiffness, and friction torque of all three models show a steady decreasing trend. The gas leakage rate of the three groove models increases with the pressure differential, film thickness, and eccentricity rate. Therefore, we can see that micro gap is the primary condition for generating hydrodynamic effects, and high-speed, high differential pressure, and large eccentricity rate have a positive effect on improving hydrodynamic effects and enhancing gas film stability, but it will lead to some leakage.

(4) The comprehensive sealing performance of the straight groove gas film model is superior to that of the no-groove and the T-groove gas film model because the straight dynamic pressure groove is a single channel. When the gas film rotates with the axis, high-speed gas is easier to pump into the dynamic pressure groove and flow into the root of the groove bottom than the two other models, which is blocked by the dam zone and weir zone, creating a pressure boosting effect, and quickly forming a strong hydrodynamic effect. This can improve gas film buoyancy and gas stability, enhance sealing performance, and reduce leakage.

9. Patents

The cylindrical gas film sealing structure used in the study was designed by the authors, and it has been applied for a patent and authorized. The patent name is "a double acting flexible support dry gas sealing device with end face and cylinder surface combination." The patent number is ZL201822008358.5.

Author Contributions: Conceptualization, Z.X.; Data curation, L.X.; Investigation, J.S., M.L., T.L. and X.H.; Methodology, Z.X., J.S. and X.H.; Resources, Z.X.; Software, J.S. and Z.X.; Writing—original draft, Z.X., J.S. and T.L.; Writing—review and editing, Z.X., L.X., M.L. and X.H. All authors have read and agreed to the published version of the manuscript.

Funding: This research was funded by the National Natural Science Foundation of China, grant number 51765024. The research was also funded by the key project of Yunnan Provincial Department of Science and Technology—Research on non-invasive detection mechanism and characteristics of microplastics based on frictional volt effect KKSD202301007.

Data Availability Statement: All data have been included in this article.

Acknowledgments: We gratefully acknowledge the Extreme Sealing Laboratory for providing the necessary equipment for this study. We would like to thank Li and Wang for their valuable contributions to this research.

Conflicts of Interest: The authors declare no conflict of interest.

References

1. Chupp, R.E.; Hendricks, R.C.; Lattime, S.B.; Steinetz, B.M. Sealing in turbomachinery. *J. Propuls. Power* **2006**, *22*, 313–349. [CrossRef]
2. Hendricks, R.C.; Tam, L.T.; Muszynska, A. Turbomachine sealing and secondary flows. In Proceedings of the Second International Symposium on Stability Control of Rotating Machinery, NASA/TM-2004-211991/PT2. Gdansk, Poland, 4–8 August 2003.
3. Laxander, A.; Fesl, A.; Hellmig, B. Development and Testing of Dry Gas Seals for Turbomachinery in Multiphase CO_2 Applications. In Proceedings of the 3rd European Supercritical CO_2 Conference, Paris, France, 19–20 September 2019.
4. Cao, S.; Chen, Y. A review of modern rotor/seal dynamics. *Eng. Mech.* **2009**, *26*, 68–79.
5. Steinetz, B.M.; Hendricks, R.C. Engine seal technology requirements to meet NASA's Advanced Subsonic Technology program goals. *J. Propuls. Power* **1996**, *12*, 786–793. [CrossRef]
6. Tseng, T.W.; McNickle, A.D.; Steinetz, B.M.; Turnquist, N. Aspirating seal GE90 test. In *2001 NASA Seal/secondary Air System Workshop, Volume 1*; Cleveland, Ohio; 2002; Volume 1, pp. 79–93. Available online: https://ntrs.nasa.gov/api/citations/20020091964/downloads/20020091964.pdf (accessed on 30 November 2023).
7. Ma, G.; Sun, X.; Luo, X.; He, J. Numerical simulation analysis of steady-state properties of gas face and cylinder film seal. *J. Beijing Univ. Aeronaut. Astronaut.* **2014**, *40*, 439–443.
8. Ma, G.; He, J.; Li, X.; Shen, X. Numerical calculation of dynamic characteristic coefficient of gas film seal. *J. Mech. Eng.* **2013**, *49*, 55–62. [CrossRef]
9. Ma, G.; Li, X.; Shen, X.; Hu, G. Analysis of performance and interface structure of cylinder gas film seal. *J. Aerosp. Power* **2011**, *26*, 2610–2626.
10. Su, Z.; Liu, M. CFD numerical simulation of cylinder gas film seal properties. *Lubr. Eng.* **2016**, *41*, 49–53.
11. Sedy, J. New self-aligning mechanism for the spiral-groove gas seal stability. *Lubr. Eng.* **1980**, *36*, 592–598.
12. Song, L. Current Development of Dry Gas Seal Used with Large Diameter Shaft at Home and Abroad and Application in China. *Process Equip. Pip* **2016**, *43*, 39–42, 73.
13. Zhang, D. Cylindrical Gas Film Dynamic Pressure Sealing Micro-Gap Flow Field Simulation and Test. Ph.D. Thesis, Lanzhou University of Technology, Lanzhou, China, 2019.
14. Bahukudumbi, P.; Beskok, A. A phenomenological lubrication model for the entire Knudsen regime. *J. Micromech. Microeng.* **2003**, *13*, 873–884. [CrossRef]
15. Nagai, K.; Kaneko, S.; Taura, H.; Watanabe, Y. Numerical and Experimental Analyses of Static Characteristics for Liquid Annular Seals with Helical Grooves in Seal Stator. *J. Tribol.* **2017**, *9*, 1–77. [CrossRef]
16. Lu, J.; Zhang, W.; Xie, F.; Jiao, Y. Performance analysis of gas film of adaptive cylindrical seal. *CIESC J.* **2020**, *71*, 346–354.
17. Jiang, J.; Chen, Y.; Xu, Q.; Li, J.; Peng, X. Evolution Rule and Working Applicability of Typical Derived Structures of Spiral Groove Dry Gas Seal. *Tribology* **2018**, *38*, 264–273.
18. Ding, J. Numerical Simulation and Experiment of Gas Film Flow Field on the Surface of Floating Ring Micro Groove Hydrodynamic Seal. Ph.D. Thesis, Lanzhou University of Technology, Lanzhou, China, 2019.
19. Ding, X.; He, Z.; Zhang, W.; Lu, J.; Miao, C. Parameters analysis of steady micro-scale flow of cylindrical spiral groove dry gas seal. *J. Chem. Ind. Eng.* **2018**, *4*, 1537–1546.
20. Zhao, C.; Liu, M.; Sun, J.; Wei, Q.; Xu, D. Research on mechanical properties of cylindrical gas film sealed bubbling supporting structure. *Agric. Equip. Veh. Eng.* **2021**, *59*, 32–37.
21. Sun, J.; Liu, M.; Xu, Z.; Liao, T. Research on operating parameters of T-groove cylindrical gas film seal based on computational fluid dynamics. *Adv. Compos. Lett.* **2019**, *28*, 1–7. [CrossRef]
22. Sun, J.; Liu, M.; Xu, Z.; Liao, T.; Hu, X.; Li, Y.; Wang, J. Coupled Fluid–Solid Numerical Simulation for Flow Field Characteristics and Supporting Performance of Flexible Support Cylindrical Gas Film Seal. *Aerospace* **2021**, *8*, 97. [CrossRef]
23. Hou, G.; Su, H.; Chen, G. An analysis method for the performance of compliant cylindrical intershaft gas film seal considering centrifugal expansion effect. *Proc. Inst. Mech. Eng. Part C J. Mech. Eng. Sci.* **2022**, *236*, 2728–2739. [CrossRef]

24. Hou, G.; Su, H.; Huang, Y.; Chen, C. An analysis method of pressure characteristic for cylindrical intershaft gas film seal considering centrifugal expansion, rotor misalignment, and precession. *Proc. Inst. Mech. Eng. Part J J. Eng. Tribol.* **2022**, *236*, 935–945. [CrossRef]
25. Wang, Y.; Xie, F.; Xie, X.; Wang, Y. Research on sealing performance improvement and functional rule of diversion texture at bottom of cylindrical gas film seal groove. *J. Xi'an Univ. Technol.* **2023**, *4*, 1–9.